Electronic Supplementary Information: Insights into how the aqueous environment influences the kinetics and mechanisms of heterogeneously-catalyzed CH_3OH^* and COH^* dehydrogenation reactions on Pt(111)

Cameron J. Bodenschatz, Tianjun Xie[‡], Xiaohong Zhang[‡], and
Rachel B. Getman[*]

Chemical and Biomolecular Engineering Department, Clemson
University, Clemson, South Carolina 29634, USA

S1 Introduction

Toward a better molecular-level understand of the mechanisms of heterogeneously-catalyzed reactions under an aqueous environment, we apply a combined classical molecular dynamics (cMD) and density functional theory (DFT) method to study chemical thermodynamics and kinetics. This method relies on cMD simulations to generate ensembles of liquid water configurations surrounding the catalytic reaction intermediates and transition states on the catalyst surface, and DFT to calcu-

---

[‡] These authors contributed equally to this work.
[*] Corresponding author; E-mail: `rgetman@g.clemson.edu`

late quantum chemical energies for these configurations. We apply this cMD-DFT method to the following chemical reactions, (S1)–(S11):

For hydroxymethylidyne, the "direct" dehydrogenation is

$$\mathrm{COH^* + {*} \longrightarrow CO^* + H^*} \tag{S1}$$

where a * indicates a vacant binding site on the Pt(111) surface and *'ed species are catalytic intermediates. This is also stoichiometrically equivalent to the total COH* dehydrogenation reactions when H_2O mediates the reaction. There are two routes of "H_2O-mediated" COH* dehydrogenation that we consider: (a) "H_2O-co-catalyzed" and (b) "H_2O-assisted". Both of these routes begin with "complexation" step where a water molecule forms a hydrogen-bond with an adsorbed COH* to form a $\mathrm{COH{-}H_2O^*}$ complex. It's possible that the H_2O in this complex contains a "dangling" H that points toward the Pt(111) surface or not, but in both cases it's possible that the other H atom participates in hydrogen-bonding with surrounding liquid water molecules. The case *with* a dangling H atom is written as

$$\mathrm{COH^* + H_2O \longrightarrow COH{-}H_2O^*(d)} \tag{S2a}$$

where (d) indicates the presence of a dangling H atom, and the more general case *without* a dangling H is written as

$$\mathrm{COH^* + H_2O \longrightarrow COH{-}H_2O^*} \tag{S2b}$$

From the complex, the dehydrogenation reaction can proceed through the H_2O-co-catalyzed route if there is a dangling H (i.e., reaction (S2a)), which is written as

$$\mathrm{COH{-}H_2O^* + {}^* \longrightarrow CO^* + H^* + H_2O} \tag{S3}$$

reaction (S2a) and reaction (S3) sum to give the “overall” net H_2O-co-catalyzed reaction, which is written as

$$\mathrm{COH^* + {}^* \xrightarrow{H_2O} CO^* + H^*} \tag{S2a+S3}$$

Alternatively, if the $COH{-}H_2O^*$ complex interacts with the aqueous environment hydrogen-bonding network (which can occur from a complex *with* or *without* a dangling H) it can undergo another complexation reaction to form a $COH{-}H_2O{-}H_2O^*$ complex, i.e.

$$\mathrm{COH{-}H_2O^* + H_2O \longrightarrow COH{-}H_2O{-}H_2O^*} \tag{S4}$$

which can then lead to dehydrogenation of the COH^* molecule via the H_2O-assisted route to form CO^* and H_5O_2, i.e.

$$\mathrm{COH{-}H_2O{-}H_2O^* \longrightarrow CO^* + H_5O_2} \tag{S5}$$

Solvated proton complexes have been shown in the literature with the general chemical formula $H_{2n+1}O_n$, where n indicates the number of water molecules solvating the proton, including hydronium complex (H_3O),[1–11] Zundel complex (H_5O_2),[2,4–7,9–15] and Eigen complex (H_9O_4).[5–7,9] In this work we only consider the case where $n = 2$ and a Zundel complex is formed. Reactions (S2), (S4), and (S5) can be summed into a net H_2O-assisted reaction, i.e.

$$\mathrm{COH^* + 2H_2O \longrightarrow CO^* + H_5O_2} \tag{S2+S4+S5}$$

Similar reaction equations can be written for CH_3OH^*. For example, the direct dehydrogenation for CH_3OH^* is

$$\mathrm{CH_3OH^* + {*} \longrightarrow CH_2OH^* + H^*} \tag{S6}$$

Similar complexation reactions to those for COH* can occur for CH_3OH^*, i.e. the case *with* a dangling H is written as

$$\mathrm{CH_3OH^* + H_2O \longrightarrow CH_3OH{-}H_2O^*(d)} \tag{S7a}$$

and the case *without* the dangling H is written as

$$\mathrm{CH_3OH^* + H_2O \longrightarrow CH_3OH{-}H_2O^*} \tag{S7b}$$

Reaction (S7a) can lead to H_2O-co-catalyzed dehydrogenation, i.e.

$$\mathrm{CH_3OH{-}H_2O^* + {*} \longrightarrow CH_2OH^* + H^* + H_2O} \tag{S8}$$

Reaction (S7a) and reaction (S8) sum to give the overall net H_2O-co-catalyzed reaction, which is written as

$$\mathrm{CH_3OH^* + {}^* \xrightarrow{H_2O} CH_2OH^* + H^*} \tag{S7a+S8}$$

However, we found reaction (S7a) to have a very low pre-exponential factor, implying a low probability of configurations that would facilitate reaction (S8) forming. Additionally, transition state (TS) searches for reaction (S8) converged to TS structures for reaction (S6) instead, where H_2O was not facilitating the reaction. Instead, the methyl H rotated toward the Pt(111) surface and transferred directly from CH_3OH^* to the surface. Even if this reaction occurred, we would expect it to have a high barrier. For these reasons, reaction (S8) was neglected from the main text.

CH_3OH^* can also follow the H_2O-assisted route like COH^* by undergoing a second complexation reaction, i.e.

$$\mathrm{CH_3OH{-}H_2O^* + H_2O \longrightarrow CH_3OH{-}H_2O{-}H_2O^*} \tag{S9}$$

and then dehydrogenation to form an H_5O_2, i.e.

$$\mathrm{CH_3OH{-}H_2O{-}H_2O^* \longrightarrow CH_2OH^* + H_5O_2} \tag{S10}$$

Again, the complexation reactions and H_2O-assisted dehydrogenation reaction can sum to give a net reaction of

$$CH_3OH^* + 2H_2O \longrightarrow CH_2OH^* + H_5O_2 \tag{S7+S9+S10}$$

Finally, to complete the H_2O-assisted reaction routes for both the CH_3OH^* and COH^* reaction intermediates, the H_5O_2 that is formed must dehydrogenate by depositing a H atom on the Pt surface, i.e.

$$H_5O_2 + * \longrightarrow 2H_2O + H^* \tag{S11}$$

Summing this reaction with the net reactions (S2+S4+S5) and (S7+S9+S10) yields stoichiometrically equivalent overall reactions as reaction (S1) and (S6), respectively.

S1.1 Interaction energy

Previous work in our group[16] showed that, when calculating the interaction energy for 44 different oxy-hydrocarbon adsorbates on Pt(111) using an LJ + C non-bonding potential, there was almost no difference between the interaction energy calculated using 10 water configurations and that calculated using 30,000 water configurations. While this result was calculated using a classical potential, the authors also showed that the difference between the interaction energy calculated using a classical and using DFT was almost constant, indicating that the same trend for the interaction energies calculated with different numbers of water configurations should hold if the interaction energy was calculated using

DFT. Therefore, all interaction energies in this work are calculated using 10 water configurations per reaction intermediate or TS complex.

For all reactions where the 95% confidence interval in the interaction energy is greater than the 95% confidence interval in the calculated activation barriers from multiple initial geometries, only water configurations from one initial geometry were used. The only reaction where this was not the case (i.e., the 95% confidence interval in the calculated activation barrier over multiple TS geometries was greater than the 95% confidence interval in the interaction energy) was reaction (S6), so water configurations generated from multiple initial TS geometries were used. In the case of reaction (S6), the activation barrier, the 10 total water configurations were obtained by selecting at least 2 water configurations from the MD trajectory over each initial geometry due to slight variations in the TS complex geometries under different liquid water configurations.

We also compare these ΔE_{int} values calculated using the cMD-DFT method as presented in the main text to ΔG_{sol} values calculated using the VASPSol implicit solvation model.[17] These results are seen in Table S1.

Table S1: A comparison of ΔE_{int} values calculated using the cMD-DFT method to ΔG_{int} values calculated using the VASPSol implicit solvation model.

Adsorbate	ΔE_{int}(cMD-DFT) [eV]	ΔG_{sol}(VASPSol) [eV]
COH*	-0.70 ± 0.07	-0.31
CO*	-0.03 ± 0.03	-0.04
$COH{-}H_2O$*	-0.55 ± 0.09	-0.27
$COH{-}H_2O{-}H_2O$*	-1.07 ± 0.17	-0.36
CH_3OH*	-0.48 ± 0.18	-0.28
CH_2OH*	-0.64 ± 0.12	-0.19
$CH_3OH{-}H_2O$*	-1.29 ± 0.20	-0.55
$CH_3OH{-}H_2O{-}H_2O$*	-1.27 ± 0.29	-0.61
H*	0.00 ± 0.00	0.00
H_2O	-0.28 ± 0.10	-0.25
H_5O_2	-1.50 ± 0.31	-1.28

S2 Hydrogen bonding criteria and examples

In this work we consider structures where water can act as a hydrogen-bond donor, i.e. where a water hydrogen atom is pointed at the oxygen atom of the adsorbate, and as a hydrogen-bond acceptor, i.e. where the hydrogen of adsorbate hydroxyl group is pointed at the oxygen atom of a water molecule. We consider a water molecule to be a hydrogen bond donor if the O_{H_2O}—O_{Ads} distance is ≤ 3.5 Å and if the O_{Ads}—O_{H_2O}—H_{H_2O} angle is $\leq 30°$. An example of structure where water is a hydrogen-bond donor is shown in Figure S1a. We consider a water molecule to be a hydrogen bond acceptor if the O_{H_2O}—O_{Ads} distance is ≤ 3.5 Å and if the H_{Ads}—O_{Ads}—O_{H_2O} angle is $\leq 30°$. An example of structure where water is a hydrogen-bond acceptor is shown in Figure S1b.

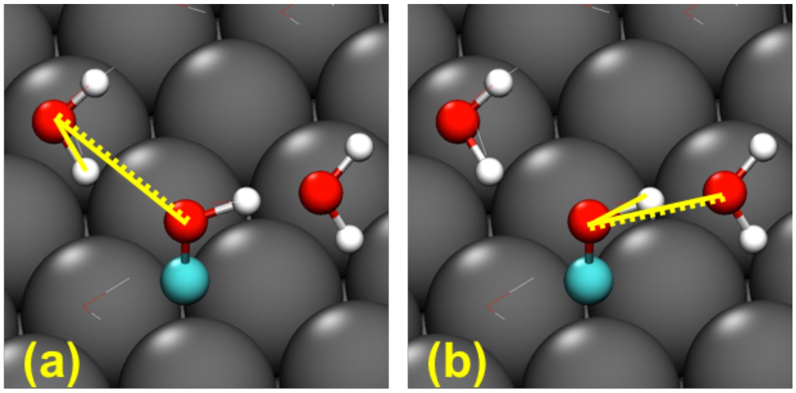

Figure S1: Example configurations of COH* where the H_2O acts as a (a) hydrogen-bond donor and (b) hydrogen-bond acceptor. In both cases, we require that the O_{COH^*}—O_{H_2O} distance (indicated by the dashed line) be ≤ 3.5 Åand the O−O−H angle (indicated by the solid lines) be $\leq 30°$. Pt = gray, C = teal, O = red, H = white. Water molecules that are not hydrogen-bonded to COH* are shown as lines for visual clarity.

An example of COH* and a hydrogen-bonded H_2O *with* a dangling H atom and an example *without* a dangling H atom are shown in Figure S2a and S2b, respectively. In Figure S2a, the dangling H atom is ≤ 2.5 Å from the plane of the Pt(111) surface and is pointing down toward the surface (i.e., it is closer to the Pt surface than the O atom in the same H_2O molecule). In both cases, it is possible for the H_2O molecule to hydrogen-bond with other liquid H_2O molecules.

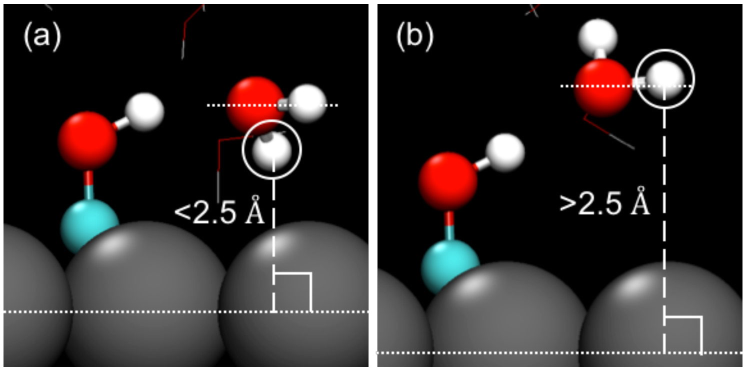

Figure S2: COH* with a hydrogen-bonded H_2O in configurations where the H_2O (a) has a dangling H atom and (b) does not have a dangling H atom. The distance used to determine whether the H was ≤ 2.5 Å from the Pt surface was that measured from the circled H. The dotted lines indicate the plane of the Pt(111) surface and the plane of the O atom parallel to the plane of the Pt(111) surface.

S3 Computational details for the ab initio molecular dynamics simulation

In the main text, *ab initio* molecular dynamics (AIMD) simulations were used to find structures of H_2O and H_5O_2 intermediates, as well as TS structures for COH* and H_5O_2 dehydrogenation reactions via the H_2O-assisted route. The computational details for that simulation are as follows. The simulations were performed performed with the Vienna Ab-Initio Simulation Package (VASP) code,[18–21] using a periodic plane-wave basis set with an energy cutoff of 400 eV. The Perdew, Burke, and Ernzerhof[22,23] (PBE) functional was used for electron exchange and correlation, and the projector augmented wave[24,25] (PAW) method was used to calculate interactions between the valence and core electrons. The D2 dispersion correction[26] was employed. Gaussian smearing with $\sigma = 0.1$ eV was used. The first Brillouin zone was sampled at the Gamma point only to improve the computational tractability.[27] The simulation box comprised 24 H_2O molecules over a 3-layer $p(3\times3)$ Pt(111) slab. AIMD was carried out in the NVT ensemble at 300 K with a time step of 0.5 fs and runtime of $\sim$100 ps, with data sampled every 5 fs. The temperature was maintained with a Nosé-Hoover thermostat.[28,29] The maximum number of vectors stored in the charge density mixer during an ionic step was set to 40 to approximate the charge dielectric function in the subsequent ionic step and to minimize the number of electronic iterations per ionic step. The initial configuration was taken from the production run of the analogous cMD simulation. Pt atoms were held fixed during the simulation, but the COH* and H_5O_2 intermediates and the H_2O molecules were allowed to move according to Newton's equations of motion. Animations of the AIMD simulations are available as Supplemental Videos (SV) SV1, SV2, and SV3 on the Getman Research Group GitHub page.[i]

S4 Selection of H_5O_2 and H_2O structures from AIMD

During the resulting AIMD trajectory, it was observed that the excess hydrogen interacted with either two water molecules that were both interacting with the Pt(111) surface, or with one water that was interacting with the Pt(111) surface and another that was not. We refer to these two configurations of H_5O_2 as the "parallel" configuration and the "perpendicular" configuration, respectively. The

---

[i] `https://github.com/getman-research-group/Geometry-files-for-Insights-into-how-the-aqueous-environment-influences-the-kinetics-and-mechanisms`

"parallel" configuration of H_5O_2 binds such that the two oxygen atoms are nearly in a plane parallel to the Pt surface, and the terminal hydrogen atoms bound to the oxygen atoms either both point toward the surface, both point away from the surface, or one points toward the surface and the other points away. The fifth hydrogen atom in H_5O_2 is bound between both oxygen atoms. This adsorption geometry for H_5O_2 is similar to that found previously in the literature[4]. The perpendicular configuration of H_5O_2 binds with the two oxygen atoms in a line nearly normal to the Pt surface, and the terminal hydrogen atoms bound to the oxygen atom closer to the surface generally point toward the surface while the terminal hydrogen atoms bound to the oxygen further from the surface generally point away from the surface. Similar to the parallel configuration, the fifth hydrogen atom is bound between the two oxygen atoms. We find for H_5O_2 that in the gas phase the parallel configuration ($E_{\text{bind}} = -0.60$ eV) is more thermodynamically favorable than the "perpendicular" configuration ($E_{\text{bind}} = 0.02$ eV). In the liquid phase, the perpendicular configuration has a stronger interaction energy ($E_{\text{int}} = -2.12 \pm 0.50$ eV) than the parallel configuration ($E_{\text{int}} = -1.75 \pm 0.44$ eV) and therefore both configurations have similar liquid-phase binding energies within the error bars ($E_{\text{bind}} = -2.35 \pm 0.44$ eV for the parallel configuration compared to $E_{\text{bind}} = -2.10 \pm 0.50$ eV for the "perpendicular" configuration).

Similarly, two primary configurations for H_2O molecules away from the excess hydrogen were identified from the AIMD trajectory. The parallel configuration where the H_2O molecule is nearly parallel with the Pt surface (the oxygen atom may be slightly closer to or further from the surface than the two hydrogen atoms), and the perpendicular configuration where the H_2O molecule has one hydrogen atom point toward a surface Pt atom and the other hydrogen atom pointed away from the surface. We find that in the gas phase the parallel configuration ($E_{\mathrm{bind}} = -0.47$ eV) is more thermodynamically favorable than the perpendicular configuration ($E_{\mathrm{bind}} = -0.24$ eV). In the liquid phase, the perpendicular configuration has a stronger interaction energy ($E_{\mathrm{int}} = -0.67 \pm 0.11$ eV) than the parallel configuration ($E_{\mathrm{int}} = -0.33 \pm 0.09$ eV) and therefore both configurations have similar liquid-phase binding energies within the error bars ($E_{\mathrm{bind}} = -0.80 \pm 0.09$ eV for the parallel configuration compared to $E_{\mathrm{bind}} = -0.91 \pm 0.11$ eV for the perpendicular configuration). Representative structures of these H_5O_2 and H_2O configurations are reported in Figure S3. Results reported in this work are averages of 4 structures representing each the parallel and perpendicular configurations for both H_5O_2 and H_2O. These results are summarized in Table S2. Geometry files for H_5O_2 and H_2O in the POSCAR format for the VASP are available online at the Getman Research Group GitHub page.[ii]

[ii] `https://github.com/getman-research-group/Geometry-files-for-Insights-into-how-the-aqueous-environment-influences-the-kinetics-and-mechanisms`

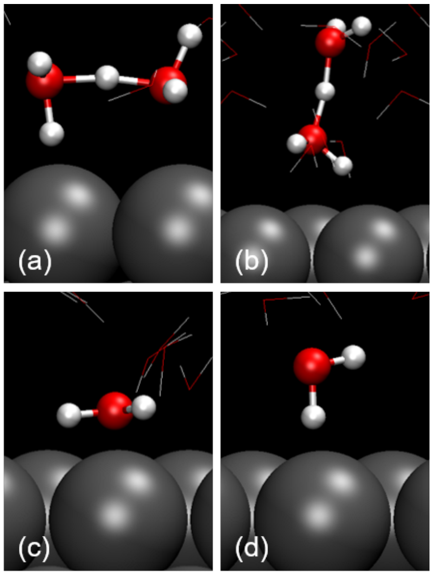

Figure S3: Side views of representative structures for the parallel and perpendicular configurations of H_5O_2 ((a) and (b), respectively) and H_2O ((c) and (d), respectively).

Table S2: Gas-phase binding energies, interaction energies, and liquid-phase binding energies for H_5O_2 and H_2O in the parallel and perpendicular configurations. All energies are reported in eV.

Adsorbate	Configuration	E_{bind}(gas)	E_{int}	E_{bind}(aq)
H_5O_2	Parallel	−0.60	−1.75 ± 0.44	−2.35 ± 0.44
	Perpendicular	0.02	−2.12 ± 0.50	−2.10 ± 0.50
H_2O	Parallel	−0.47	−0.33 ± 0.09	−0.80 ± 0.09
	Perpendicular	−0.24	−0.67 ± 0.11	−0.91 ± 0.11

S5 Molecular dynamics force field parameters

S5.1 Non-bonded interactions

Pairwise interaction energies in the classical MD simulations were calculated using a Lennard-Jones + Coulomb (LJ + C) potential (eq S12)[30]. Non-bonded interactions were calculated using equation S12.

$$E_{ij} = 4\varepsilon_{ij}\left[\left(\frac{\sigma_{ij}}{r_{ij}}\right)^{12} - \left(\frac{\sigma_{ij}}{r_{ij}}\right)^{6}\right] + \frac{Cq_iq_j}{\varepsilon r_{ij}} \tag{S12}$$

The Lennard-Jones σ and ε parameters for platinum and adsorbed hydrogen were taken from the Universal Force Field[31] (UFF), while the charges for both were set to 0. LJ and C parameters for liquid H_2O were taken from the TIP3P-CHARMM[32] model. We note that, while writing this manuscript, the GAL17 potential for modeling H_2O interactions with Pt(111) was published,[33] providing the first force field developed specifically for studying H_2O-Pt(111) interactions to our knowledge. Our ongoing work includes understanding the influence of the H_2O-Pt(111) potential on catalytic quantities. Similar to the work by Cui et. al[34], in which they used the water TIP3P parameters for H_3O^+ and modified the charges of the atoms, TIP3P-CHARMM parameters were used for H_5O_2 with the following changes: 1) for cMD simulations used to generate water configurations around reaction intermediate structures, the charge of the H that is stabilized between the two O atoms in H_5O_2 (indicated by a 1 in Figure S4) is set to 0 e^-, and 2) for cMD simulations used to generate water configurations around TS structures, the charge of the H that is being transferred from the O atom in H_5O_2 (indicated by a 2 in Figure S4) to the Pt surface is set to 0 e^-.

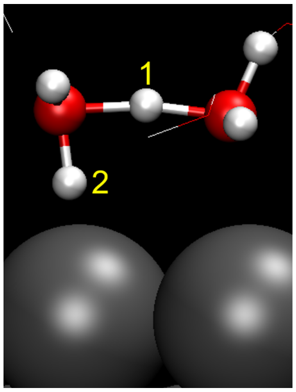

Figure S4: An example structure for H_5O_2 on Pt(111) used for to generate liquid water configurations using cMD simulations. The H atom indicated by a 2 is the H that was to be transferred to the Pt surface, and the H atom indicated by a 1 shifts from being shared between both O atoms to strictly bonding with the left O atom to form a water molecule. In cMD simulations of the H_5O_2, the H indicated by a 1 was given a charge of 0 e^-, and in cMD simulations of the TS complex after the dehydrogenation transfer began, the H indicated by a 2 was given a charge of 0 e^-.

As reported in the manuscript, when the Pt charges are set to 0 e^-, $\Delta E_{\text{int}}(\text{COH*}) = -0.70 \pm 0.07$ eV and $\Delta E_{\text{int}}(\text{CH}_2\text{OH*}) = -0.64 \pm 0.12$ eV. When Pt charges are set using DDEC charges, $\Delta E_{\text{int}}(\text{COH*}) = -0.63$ eV and $\Delta E_{\text{int}}(\text{CH}_2\text{OH*}) = -0.63$ eV.[17] DDEC charges are partial atomic charges calculated via charge partitioning of a known electron density.[35] The values calculated using DDEC charges are within the range of the error bars for the values calculated using $q(\text{Pt}) = 0$ e^-. Using DDEC charges, the largest magnitude charge on any Pt atom in the supercell with COH* is -0.09 e^-, while the largest magnitude charge on Pt in the supercell with $\text{CH}_2\text{OH*}$ is -0.08 e^-. These charges are less than the charges of the atoms in the reaction intermediates and TS complexes, which are ~ -0.6 e$^-$ for O atoms and ~ -0.3 e$^-$ for C atoms. Additionally, the distances between the water molecules and the reaction intermediate are shorter ($\sim$ 2.5 Å) than those between the water molecules and the Pt surface ($\sim$ 3 Å). Since the charges are larger for the atoms in the reaction intermediate and the distance between the water and reaction intermediate is shorter, the interaction between water and the reaction intermediate should dominate the calculation of ΔE_{int} over the interaction between water and the Pt surface.

The OPLS-AA[36] force field LJ and C parameters and atomic masses were used to for atoms in CH_3OH*, CH_2OH*, and COH*, while OPLS-AA LJ parameters for the carbon and oxygen atoms in COH* were used for CO* and the charges for these atoms were adjusted to retain a neutral molecule. Force field parameters, including Lennard-Jones coefficients, atomic charges, and atomic masses for the platinum slab, water, and all adsorbates, can be found in Table S3. Lennard-Jones coefficients for pairwise non-bonded interactions are calculated using arithmetic mixing as described by equation S13 for σ parameters and geometric mixing as described by equation S14 for ε parameters.

$$\sigma_{ij} = \frac{\sigma_i + \sigma_j}{2} \tag{S13}$$

$$\varepsilon_{ij} = \sqrt{\varepsilon_i \varepsilon_j} \tag{S14}$$

In equations S12-S14, ε_i is the depth of the Lennard-Jones potential well for atom i, ε_{ij} is the geometric average of the Lennard-Jones potential well depths of atoms i and j, σ_i is the interatomic distance where the Lennard-Jones potential is equal to 0 for atom i, σ_{ij} is the arithmetic mean of the Lennard-Jones σ's for atoms i and j, r_{ij} is the distance between atoms i and j, q_i is the charge of atom i, C is an energy-conversion constant and ε is the dielectric constant, which is set to 1.0 by default. In equation S15, k_r is the bond coefficient, r is the interatomic distance, r_{eq} is the equilibrium interatomic distance.

S5.2 Non-bonded interaction mixing rules

The OPLS-AA force field was defined using geometric mixing rules for calculating pairwise σ_{ij} and ε_{ij} coefficients from their single component coefficients[37]. However, TIP3P-CHARMM was defined using Lorentz-Berthelot mixing rules, i.e. geometric mixing for σ_{ij} and arithmetic mixing for ε_{ij}[30]. Therefore, there is ambiguity in how to mix parameters for water-adsorbate interactions, since the mixing rules for each set of parameters are different. Since ε_{ij} is calculated using geometric mixing in both force fields, the potential energy well depth will be the same between the two; however, σ_{ij} is calculated using geometric mixing in OPLS-AA and arithmetic mixing in TIP3P-CHARMM, so the interatomic distance of zero potential will be different. An example of this is interactions between the hydroxyl hydrogen of the adsorbate molecule and a water oxygen: for the hydroxyl H of both CH_3OH* and COH*, $\sigma_i = 0.0$ Å, and for water O, $\sigma_i = 3.1507$ Å, using the geometric mixing rules, $\sigma_{ij} = 0.0$, and using arithmetic mixing rules, $\sigma_{ij} = 1.5754$ Å.

We tested the use of different mixing rules on the creation of liquid water structures for our simulations. We ran MD simulations using various mixing rules for calculating the pairwise σ_{ij} terms for each set atoms: one simulation used arithmetic mixing for all σ_{ij} values, one used geometric mixing for all σ_{ij} values, one used arithmetic mixing to calculate σ_{ij} for water-water and water-adsorbate interactions and geometric mixing for adsorbate-adsorbate interactions, and finally one used arithmetic mixing to calculate σ_{ij} for water-water interactions and geometric mixing for water-adsorbate and adsorbate-adsorbate interactions. We then calculated the average number of hydrogen bonds formed, the average O—O distance, and the average O—O—H angle. The results for these test calculations are shown in Figures S5–S7, and show that there is no statistically significant difference in these values based on the mixing rules used, and therefore there is not a significant difference in the water structure generated from our MD simulations based on the mixing rules used.

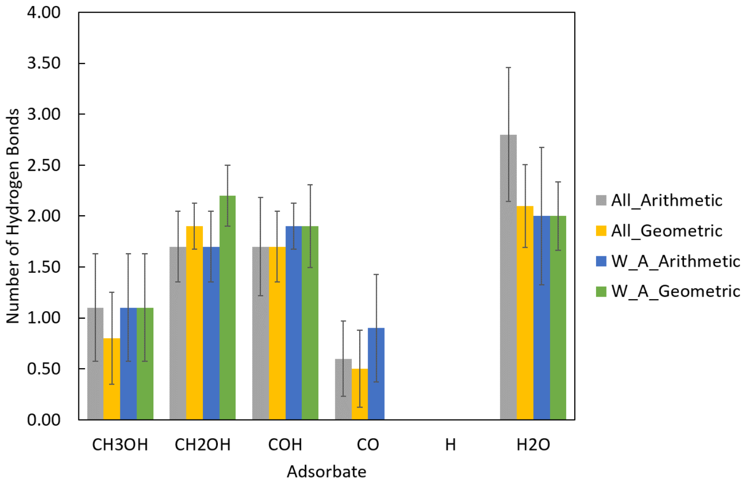

Figure S5: The average number of hydrogen bonds for CH_3OH*, CH_2OH*, COH*, CO*, H*, and H_2O calculated using arithmetic mixing for calculating all pairwise σ_{ij} values ("All_Arithmetic"), geometric mixing for calculating all pairwise σ_{ij} values ("All_Geometric"), arithmetic mixing for calculating σ_{ij} for water—water and water—adsorbate interactions and geometric mixing for adsorbate—adsorbate interactions ("W_A_Arithmetic"), and arithmetic mixing rules for calculating σ_{ij} for water—water interactions and geometric mixing for water—adsorbate and adsorbate—adsorbate interactions ("W_A_Geometric").

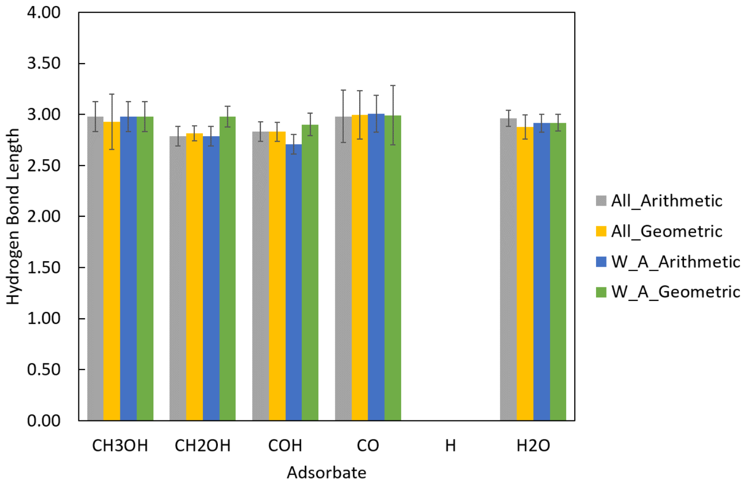

Figure S6: The average hydrogen bond O—O distance for CH_3OH^*, CH_2OH^*, COH*, CO*, H*, and H_2O calculated using arithmetic mixing for calculating all pairwise σ_{ij} values ("All_Arithmetic"), geometric mixing for calculating all pairwise σ_{ij} values ("All_Geometric"), arithmetic mixing for calculating σ_{ij} for water—water and water—adsorbate interactions and geometric mixing for adsorbate—adsorbate interactions ("W_A_Arithmetic"), and arithmetic mixing rules for calculating σ_{ij} for water—water interactions and geometric mixing for water—adsorbate and adsorbate—adsorbate interactions ("W_A_Geometric").

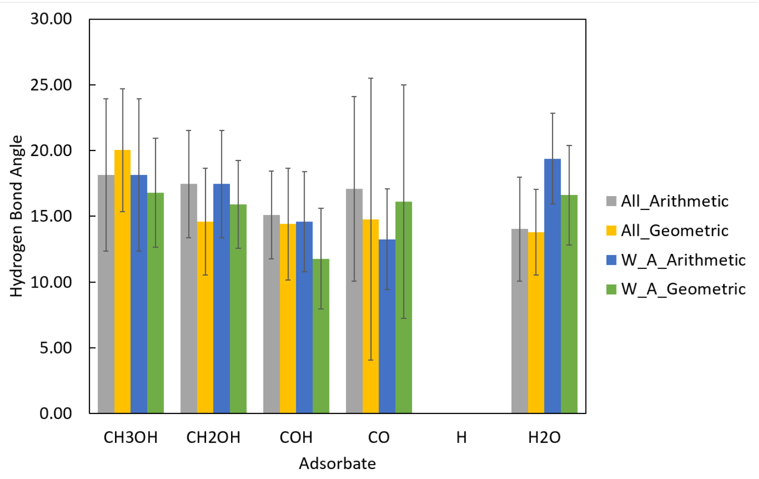

Figure S7: The average hydrogen bond O—O—H angle for CH_3OH*, CH_2OH*, COH*, CO*, H*, and H_2O calculated using arithmetic mixing for calculating all pairwise σ_{ij} values (“All_Arithmetic”), geometric mixing for calculating all pairwise σ_{ij} values (“All_Geometric”), arithmetic mixing for calculating σ_{ij} for water—water and water—adsorbate interactions and geometric mixing for adsorbate—adsorbate interactions (“W_A_Arithmetic”), and arithmetic mixing rules for calculating σ_{ij} for water—water interactions and geometric mixing for water—adsorbate and adsorbate—adsorbate interactions (“W_A_Geometric”).

S5.3 Bonded interactions

Water molecules were allowed to be flexible through the use of the flexible TIP3P-CHARMM potential. Intramolecular bond interactions for H_2O were calculated using equation S15

$$E_{bond} = k_r \left(r - r_{eq}\right)^2 \tag{S15}$$

and S16[38]. In equation S16, k_θ is the angle coefficient, θ is the interatomic angle, and θ_{eq} is the equilibrium interatomic angle. The bond coefficient, $k_{r,\mathrm{OH}}$, used for TIP3P-CHARMM water was 450 kcal/mol-Å and the equilibrium bond length,

$r_{eq,\mathrm{OH}}$ was 0.9572 Å [32]. The angle coefficient, $k_{\theta,\mathrm{HOH}}$ was 55.0 kcal/mol-Å and the equilibrium angle, $\theta_{eq,\mathrm{HOH}}$ was 104.42° [32]. All other atoms, including the Pt(111) surface, the adsorbed methanol fragment, and any adsorbed water molecules that were involved in the hydrogen transfer reactions were held fixed and therefore no bonded interaction parameters were used for those atoms.

$$E_{angle} = k_\theta \left(\theta - \theta_{eq}\right)^2 \tag{S16}$$

Group	Element	Force Field	m_i [g/mol]	q_i [e$^-$]	σ_i [Å]	ε_i [kcal/mol]
Slab	Pt	UFF	195.084	0.0000	2.7540	0.0800
H_2O	O	TIP3P-CHARMM	15.9994	-0.8340	3.1507	0.1521
	H	TIP3P-CHARMM	1.00794	0.4170	0.4000	0.0460
H_5O_2	O	TIP3P-CHARMM	15.9994	-0.8340	3.1507	0.1521
	H	TIP3P-CHARMM	1.00794	0.4170	0.4000	0.0460
	H ($q = 0$ e$^-$)	TIP3P-CHARMM	1.00794	0.0000	0.4000	0.0460
CH_3OH*	C	OPLS-AA	12.0107	0.1700	3.5200	0.0670
	O	OPLS-AA	15.9994	-0.6600	3.0800	0.1700
	H (bound to C)	OPLS-AA	1.00794	0.0300	2.5000	0.0300
	H (bound to O)	OPLS-AA	1.00794	0.4000	0.0000	0.0000
CH_2OH*	C	OPLS-AA	12.0107	0.2000	3.5200	0.0670
	O	OPLS-AA	15.9994	-0.6600	3.0800	0.1700
	H (bound to C)	OPLS-AA	1.00794	0.0300	2.5000	0.0300
	H (bound to O)	OPLS-AA	1.00794	0.4000	0.0000	0.0000
COH*	C	OPLS-AA	12.0107	0.1500	3.5500	0.0700
	O	OPLS-AA	15.9994	-0.5850	3.0700	0.1700
	H	OPLS-AA	1.00794	0.4350	0.0000	0.0000
CO*	C	OPLS-AA	12.0107	0.4700	3.7500	0.1050
	O	OPLS-AA	15.9994	-0.4700	2.9600	0.2100
H*	H	UFF	1.00794	0.0000	2.8860	0.0440

Table S3: Force field parameters used for all LAMMPS simulations. H atoms denoted with ($q = 0$ e$^-$) correspond to the H indicated by a 1 in Figure S4b for H_5O_2 and indicated by a 2 for the TS for H_5O_2 dehydrogenation.

S6 Flowchart for the cMD-DFT Method

Figure S8 is a flowchart depicting the procedure of the cMD-DFT method. In the first step, the reaction intermediate or TS complex is optimized on the Pt(111) surface under vacuum while the Pt atoms are held fixed. Then, water molecules are added to the simulation box. The Pt and reaction intermediate or TS complex atoms are held fixed while an NVT cMD simulation generates a trajectory of water molecule positions over the reaction intermediate or TS complex and surface. Ten frames are extracted from the cMD trajectory and the water molecules that are hydrogen-bonded to the reaction intermediate or TS complex are identified (those depicted by balls and sticks in Figure S8d). For each of the ten frames, the hydrogen-bonded water molecules are relaxed while the Pt atoms, the reaction intermediate or TS complex atoms, and all of the non-hydrogen-bonded water molecules are held fixed. Finally, single-point energy calculations are performed for the partial structures as required for the calculation of ΔE_{int}.

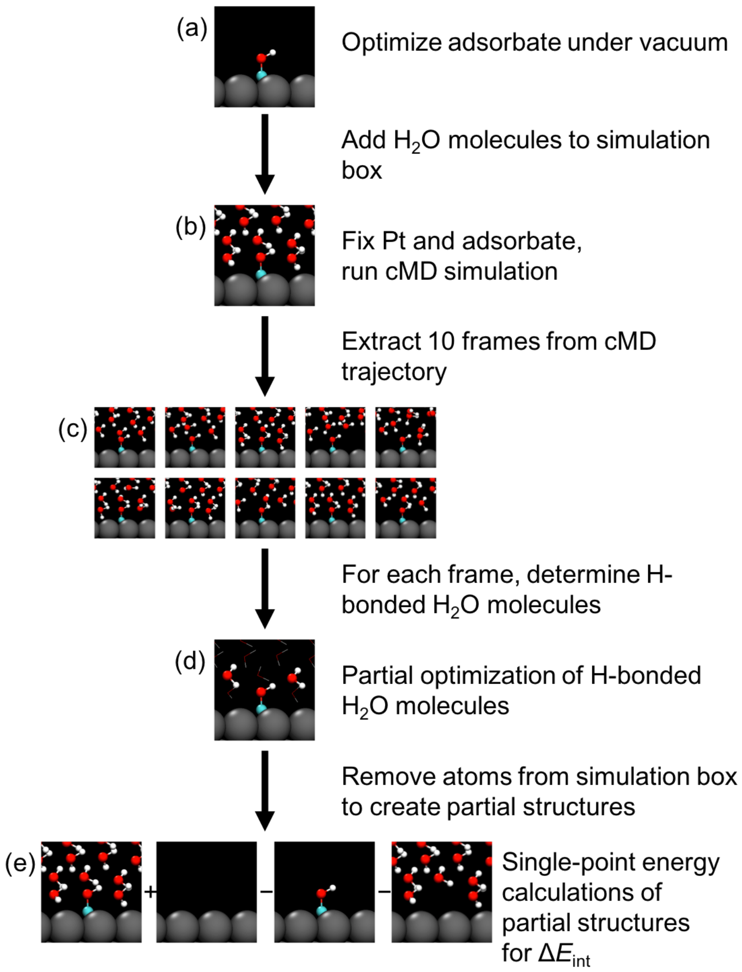

Figure S8: A flowchart depicting the cMD-DFT method described in the main text.

S7 Partial Relaxations and Interaction Energies

We conducted tests to determine the influence of which components of the system were relaxed during the partial relaxtion step in Figure S8d. First, we tested relaxing the reaction intermediate (RI) or transition state (TS) and the hydrogen-bonded H_2O molecules, while holding the non-hydrogen-bonded H_2O molecules fixed. Next, we tested relaxing only the hydrogen-bonded H_2O molecules while holding the RI or TS and all non-hydrogen bonded H_2O molecules fixed. Finally, we tested holding the entire system fixed and only performing a single-point energy calculation. The results are summarized in Table S4 below, and indicate that the influence of which atoms are included in the partial relaxation on the calculation of ΔE_{int} is small. However, when attempting to calculate the "initial state" structures for some reactions, we found that the RI would decompose readily. Therefore, to calculate the energies of intact structures of these RIs, we adopted the second method for this work.

Table S4: A comparison of ΔE_{int} values calculated when various components of the system were included in the partial relaxation step.

	ΔE_{int} [eV]		
Adsorbate	RI/TS + HB H_2O	H_2O	Single-point
COH*	-0.73 ± 0.08	-0.70 ± 0.07	-0.67 ± 0.11
CO*	-0.05 ± 0.02	-0.03 ± 0.03	-0.05 ± 0.03
CH_3OH*	-0.54 ± 0.22	-0.48 ± 0.18	-0.43 ± 0.14
CH_2OH*	-0.62 ± 0.14	-0.64 ± 0.12	-0.51 ± 0.11
H*	0.00 ± 0.00	0.00 ± 0.00	0.00 ± 0.00

S8 cMD simulations used for calculating pre-exponential terms

cMD simulations for calculating pre-exponential terms were performed slightly differently than those used in cMD-DFT.[39] Specifically, the following changes to the strategy discussed in Section 3.4.1 of the main text:

- The number of H_2O molecules in the supercell was increased from 24 to 48.

- The height of the supercell was increased to accommodate the additional H_2O molecules. This was done in a four step procedure.[39] After the H_2O molecules were added to the supercell, their positions were optimized in LAMMPS using the conjugate gradient method. The convergence criteria for this optimization were that the normalized energy ($\Delta E/E$) must fall below 1×10^{-8}, and the maximum force must fall below 1×10^{-10} kcal/mol·Å. Then, the positions of the H_2O molecules were refined in the NVT ensemble for 5 ns using global velocity rescaling and Hamiltonian dynamics to equilibrate the system. Next, a cMD simulation in the NVE ensemble was performed for 5 ns to verify that energy was being conserved. Finally, a cMD simulation in the NPT ensemble was run for 5 ns. In this simulation, only the c lattice vector was allowed to change. The pressure and temperature were maintained at 1 atm and 300 K, respectively, using a Nosé-Hoover[28,29] barostat and thermostat. During these simulations, the stress damping parameter was set to 5 ps and the temperature damping parameter was set to 100 fs. The average c lattice vector lengths from this procedure were approximately $c = 33$ Å for the different adsorbates. This yields an average water density in the bulk regions of the simulation boxes (i.e., the regions where the water densities as functions of distance from the Pt surfaces have plateaued) is approximately 1 g/cm^3 at 300 K, which compares favorably with the literature value (1.002 g/cm^3).[40]

- In the LJ+C potentials, the Coulomb terms for the Pt and adsorbate atoms used partial charges derived from the charge densities calculated in DFT. This captures the charge transfer that occurs during chemical bonding between the reaction intermediate and the Pt surface, which improves the interaction energy calculated in cMD compared to that calculated in DFT.[17] Partial charges were calculated using the density-derived electrostatic and chemical (DDEC) charge-partitioning method[35] on Pt + adsorbate systems that have been relaxed under vacuum. The Coulombic parameters calculated from the DDEC charges are listed in Table S3.

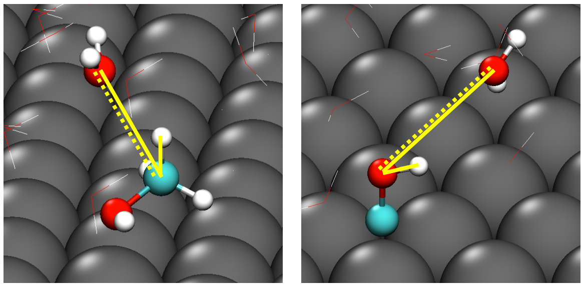

Figure S9: Distance and angle criteria used for calculation dehydrogenation frequency factors. The distance (dashed lines) must be less than 3.5 Å and the angle (solid lines) must be less than 30°. Water molecules not involved in hydrogen bonding are displayed as lines for visual clarity. Gray spheres are Pt atoms, teal spheres are C atoms, red spheres are O atoms, and white spheres are H atoms.

S9 Calculated initial state, transition state, and final state structures

S9.1 CI-NEB calculations

CI-NEB[41,42] simulations were performed as follows. First, configurations of H_2O around "initial" and "final" images were obtained using the cMD-DFT approach, with the modification that the reaction intermediates were included in the partial relaxations. Initial and final images were constant stoichiometry supercells that represented reactants and products in the elementary hydrogen transfer reactions. For example, for reaction (S1), supercells of initial images comprised a COH* intermediate, and supercells of final images comprised CO* and H* intermediates in nearest neighbor configurations. Since it was important in CI-NEB to focus the simulation on the reaction coordinate of interest, we attempted to minimize fluctuations in the H_2O structure over the course of the CI-NEB simulation as much as possible. Hence, once a H_2O configuration was selected from the many possibilities around the initial and final images, we created the corresponding final or initial image using a nearly identical configuration of H_2O molecules. Specifically, the species on the side of the reaction from which the H_2O configuration *was not* chosen was then relaxed under the selected configuration of H_2O. For example, if, for the reaction $\text{COH*} + * \longrightarrow \text{CO*} + \text{H*}$ (reaction (S1)), a configuration of H_2O was chosen around COH* (i.e., the "initial" image), then, to generate the corresponding "final" image, a CO* + H* geometry would be placed under that same H_2O configuration. The CO* and H* adsorbates, along with any

H_2O molecules that were hydrogen bonded to the original COH* adsorbate, were allowed to relax in DFT. We performed at least three CI-NEB simulations under different water configurations for each reaction.

S9.2 Structures

Converged structures for all reaction intermediates and TSs reported in the main text in the VASP POSCAR format as well as videos of the imaginary vibrational modes for TSs are available online at the Getman Research Group GitHub page.[iii]

Converged structures for the initial states (IS), TSs, and final states (FS) for reactions (S1)-(S11) are shown below in Figures S10-S27. Those atoms that make up molecules involved in the reaction either as part of the reaction intermediate or TS complex are depicted by the balls-and-sticks, while water molecules not involved in the reaction intermediate or TS complex are depicted by lines. Grey spheres are Pt atoms, teal spheres are C atoms, red spheres are O atoms, and white spheres are H atoms. Bond lengths relevant to the dehydrogenation reactions are indicated by dotted yellow lines. All lengths are in Å. Relative energies are labeled on the figures, and are all in units of eV. For our activation barrier calculations, we calculated 5 TS structures for reactions (S1) and (S6), 3 TS structures for reactions (S3) and (S10), and 1 TS structure for reactions (S5) and (S11). TS structures for reactions (S5) and (S11) were obtained directly from AIMD trajectories; therefore, CI-NEB simulations were not used to generated these TS structures and no

---

[iii] `https://github.com/getman-research-group/Geometry-files-for-Insights-into-how-the-aqueous-environment-influences-the-kinetics-and-mechanisms`

IS or FS structures are reported. We then calculated the interaction energies for these TS structures using the cMD-DFT method and sampling 10 liquid water configurations per TS structure. Videos of the imaginary vibrational modes for the TS complexes are available for download with the ESI†.

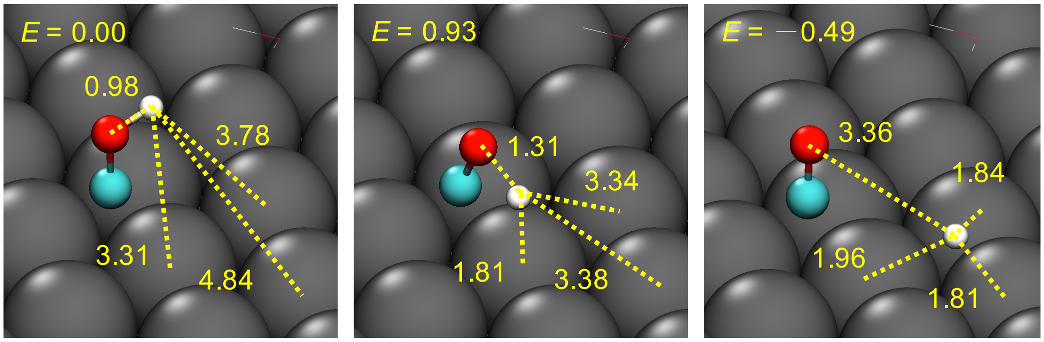

Figure S10: Initial state (left), TS (center), and FS (right) structures for reaction (S1), configuration 1. The imaginary vibrational mode for this TS complex is 195.75 meV. An animation of this vibrational mode is given in SV4.

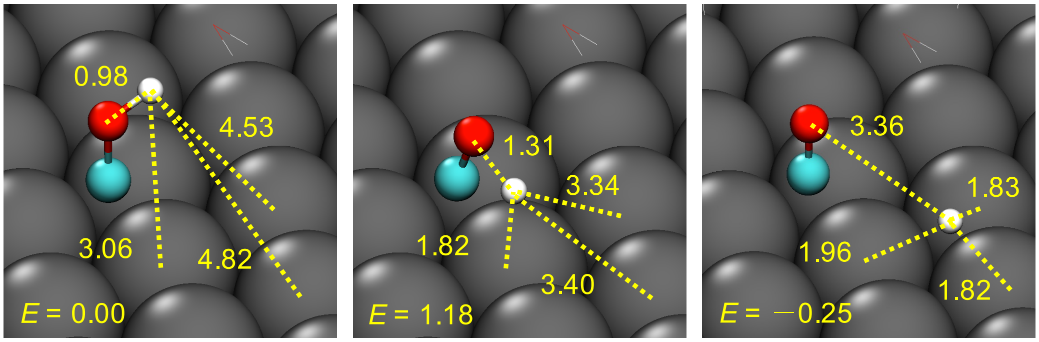

Figure S11: Initial state (left), TS (center), and FS (right) structures for reaction (S1), configuration 2. The imaginary vibrational mode for this TS complex is 196.87 meV. An animation of this vibrational mode is given in SV5.

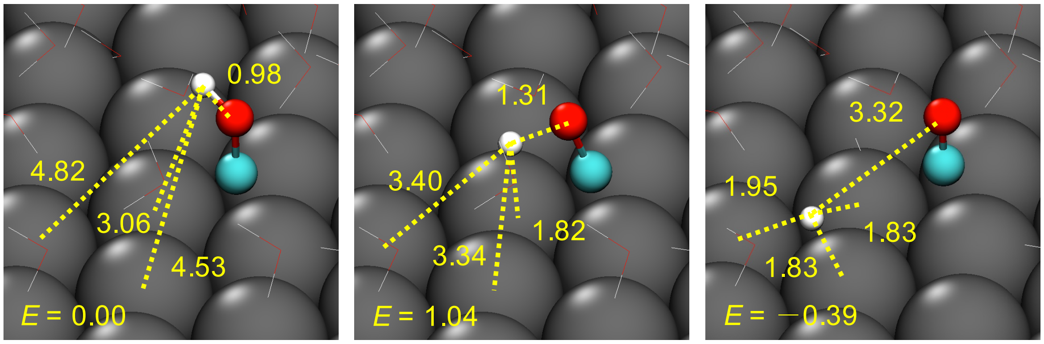

Figure S12: Initial state (left), TS (center), and FS (right) structures for reaction (S1), configuration 3. The imaginary vibrational mode for this TS complex is 198.71 meV. An animation of this vibrational mode is given in SV6.

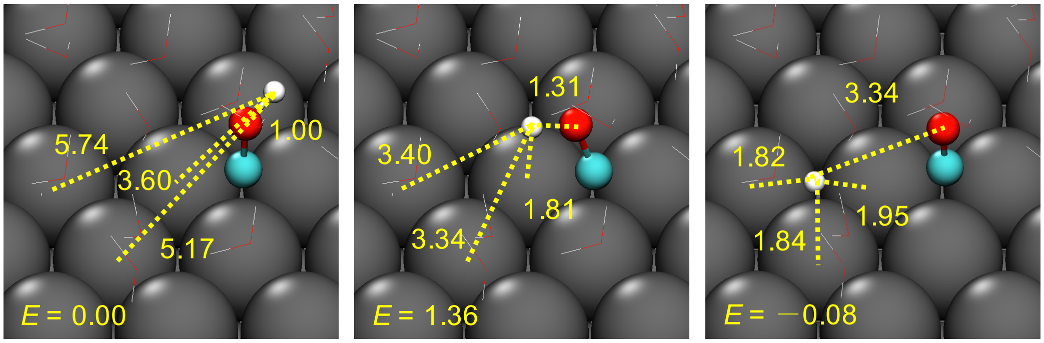

Figure S13: Initial state (left), TS (center), and FS (right) structures for reaction (S1), configuration 4. The imaginary vibrational mode for this TS complex is 193.84 meV. An animation of this vibrational mode is given in SV7.

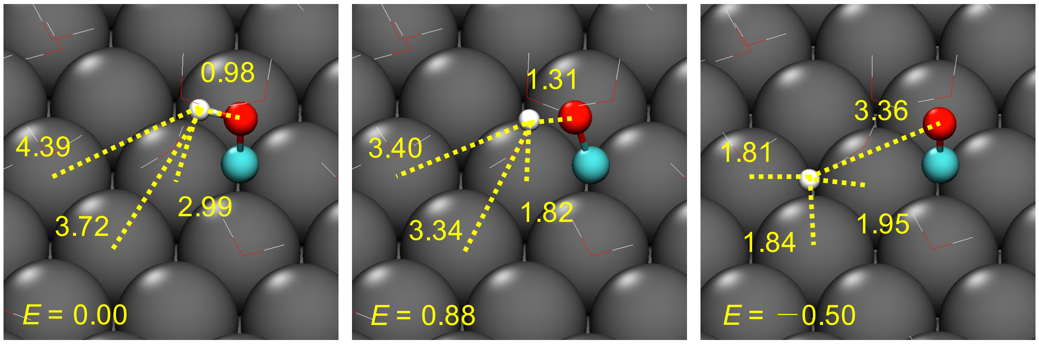

Figure S14: Initial state (left), TS (center), and FS (right) structures for reaction (S1), configuration 5. The imaginary vibrational mode for this TS complex is 197.47 meV. An animation of this vibrational mode is given in SV8.

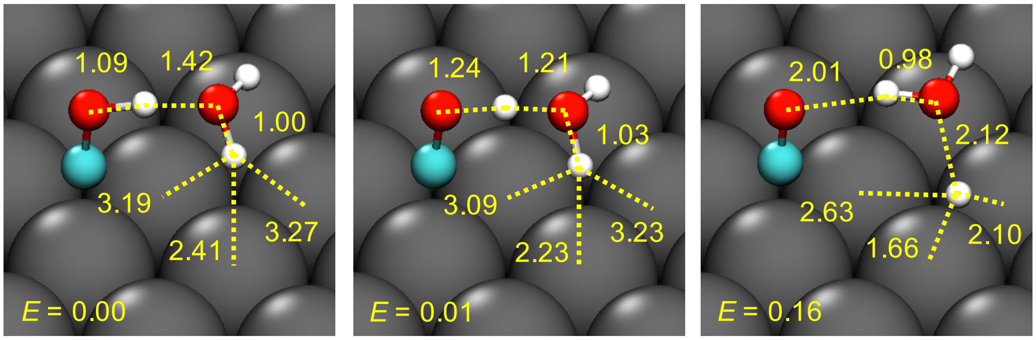

Figure S15: Initial state (left), TS (center), and FS (right) structures for reaction (S3) in the presence of only one water molecule. The imaginary vibrational mode for this TS complex is 57.19 meV. An animation of this vibrational mode is given in SV9.

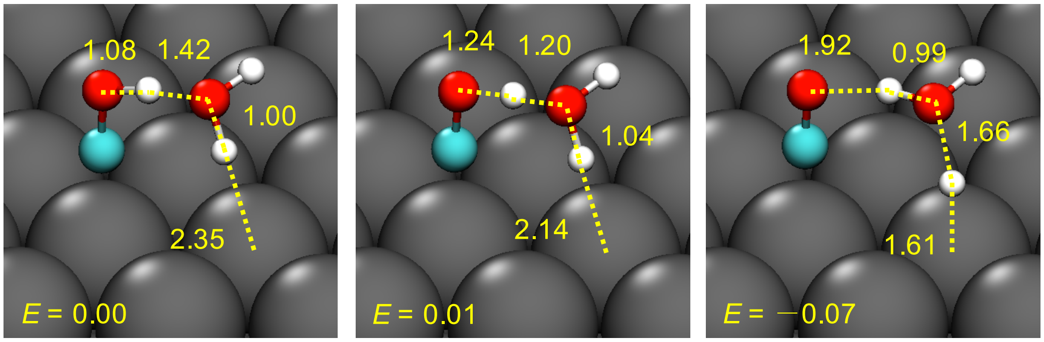

Figure S16: Initial state (left), TS (center), and FS (right) structures for reaction (S3) in the presence of only one water molecule. The imaginary vibrational mode for this TS complex is 61.05 meV. An animation of this vibrational mode is given in SV10.

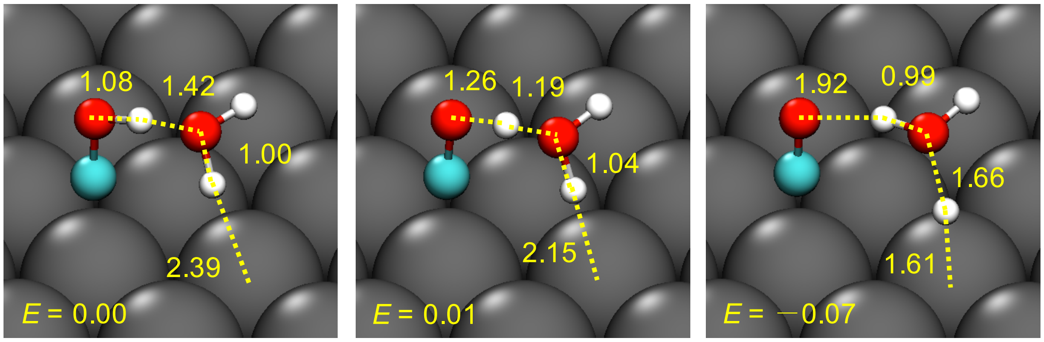

Figure S17: Initial state (left), TS (center), and FS (right) structures for reaction (S3) in the presence of only one water molecule. The imaginary vibrational mode for this TS complex is 57.59 meV. An animation of this vibrational mode is given in SV11.

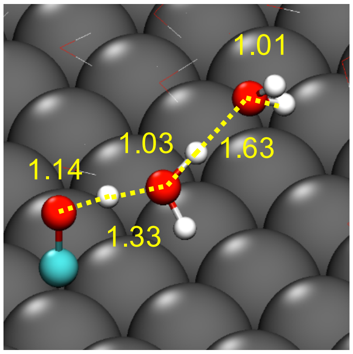

Figure S18: TS structure for reaction (S5). The imaginary vibrational mode for this TS complex is 21.35 meV. An animation of this vibrational mode is given in SV12. This structure was obtained from the AIMD trajectory shown in SV2; therefore, IS and FS structures were not generated.

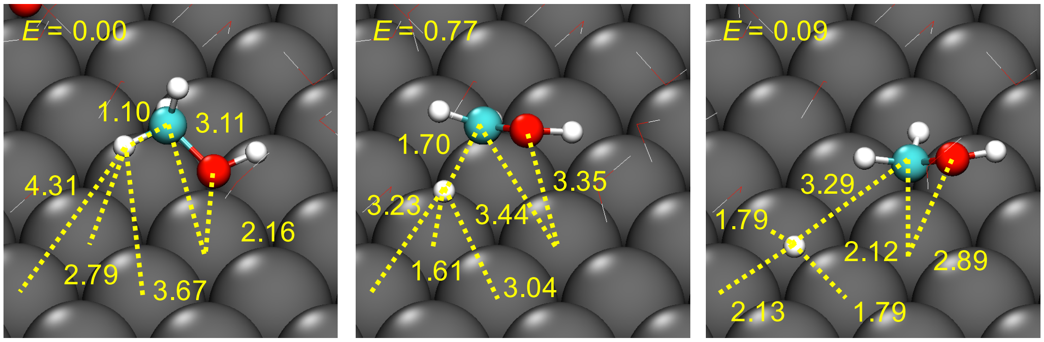

Figure S19: Initial state (left), TS (center), and FS (right) structures for reaction (S6), configuration 1. The imaginary vibrational mode for this TS complex is 29.27 meV. An animation of this vibrational mode is given in SV13.

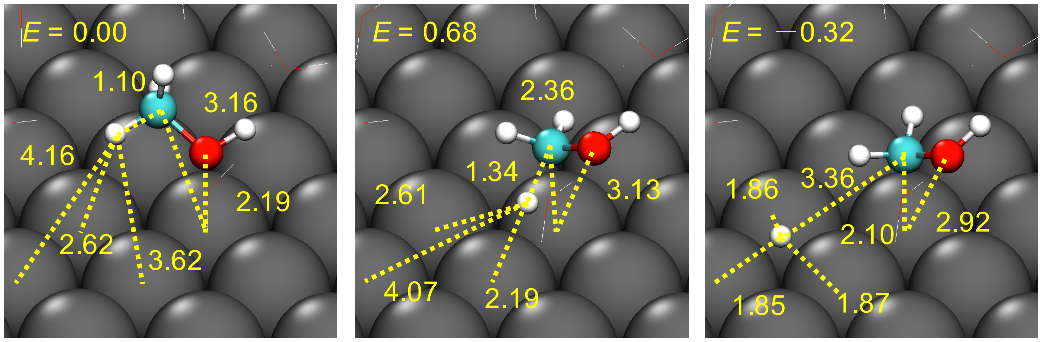

Figure S20: Initial state (left), TS (center), and FS (right) structures for reaction (S6), configuration 2. The imaginary vibrational mode for this TS complex is 58.73 meV. An animation of this vibrational mode is given in SV14.

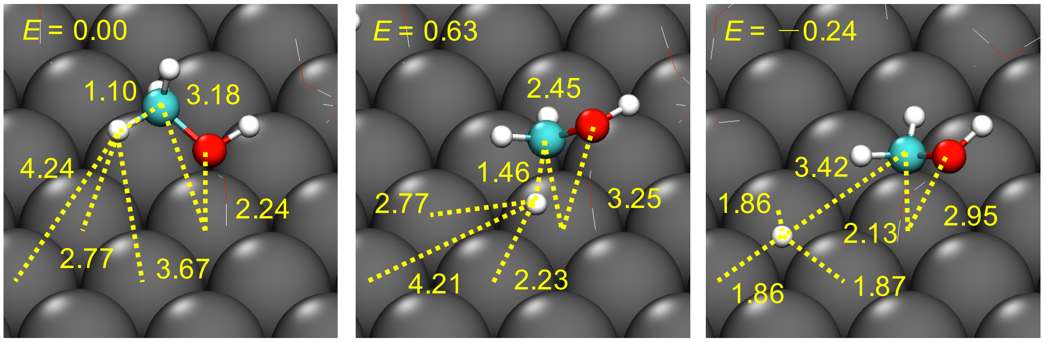

Figure S21: Initial state (left), TS (center), and FS (right) structures for reaction (S6), configuration 3. The imaginary vibrational mode for this TS complex is 94.31 meV. An animation of this vibrational mode is given in SV15.

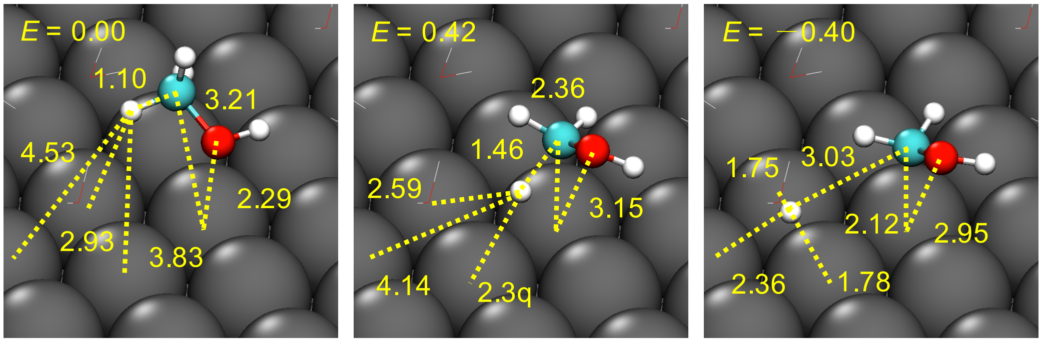

Figure S22: Initial state (left), TS (center), and FS (right) structures for reaction (S6), configuration 4. The imaginary vibrational mode for this TS complex is 98.89 meV. An animation of this vibrational mode is given in SV16.

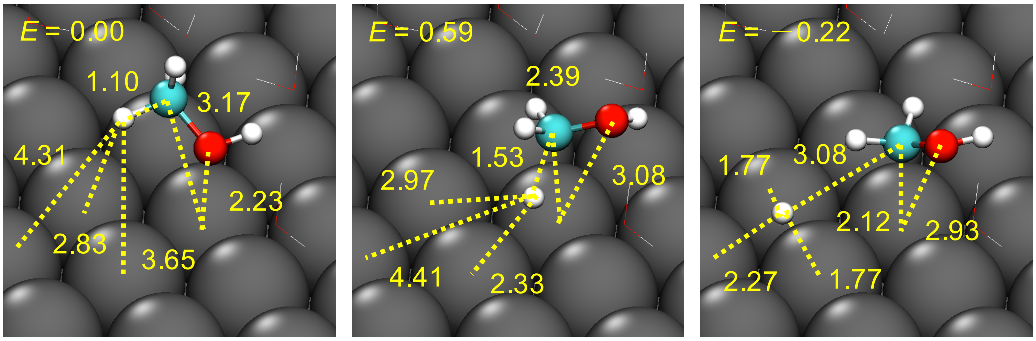

Figure S23: Initial state (left), TS (center), and FS (right) structures for reaction (S6), configuration 5. The imaginary vibrational mode for this TS complex is 98.59 meV. An animation of this vibrational mode is given in SV17.

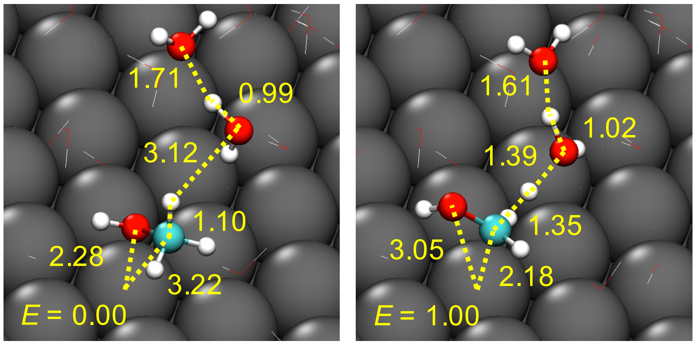

Figure S24: Initial state (left) and TS (center) structures for reaction (S10), configuration 1. The FS structure (CH_2OH^*) was not converged for this configuration. The imaginary vibrational mode for this TS complex is 104.89 meV. An animation of this vibrational mode is given in SV18.

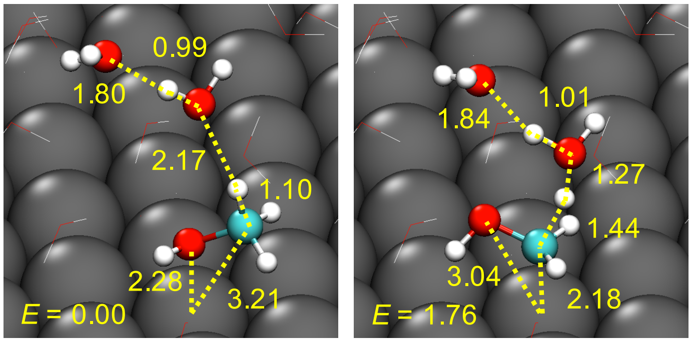

Figure S25: Initial state (left) and TS (center) structures for reaction (S10), configuration 2. The FS structure (CH_2OH^*) was not converged for this configuration. The imaginary vibrational mode for this TS complex is 118.46 meV. An animation of this vibrational mode is given in SV19.

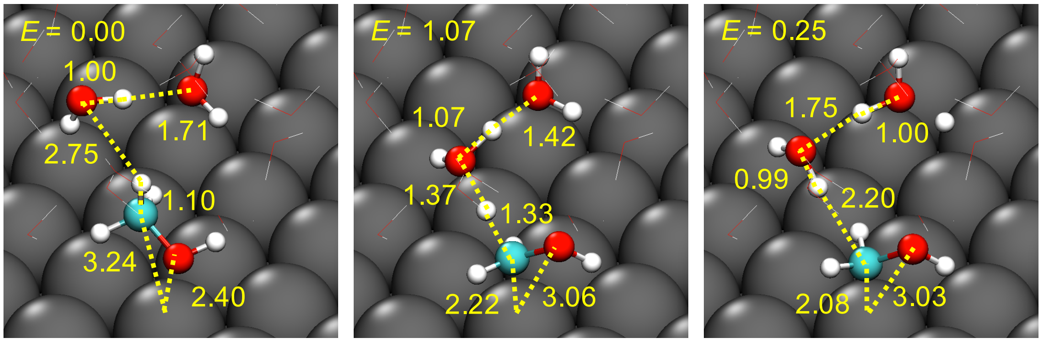

Figure S26: Initial state (left), TS (center), and FS (right) structures for reaction (S10), configuration 3. The imaginary vibrational mode for this TS complex is 114.51 meV. An animation of this vibrational mode is given in SV20.

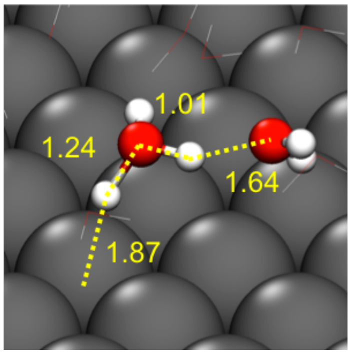

Figure S27: TS structure for reaction (S11). The imaginary vibrational mode for this TS complex is 94.26 meV. An animation of this vibrational mode is given in SV21. This structure was obtained from the AIMD trajectory shown in SV3; therefore, IS and FS structures were not generated.

S10 Solvation methods for reaction energy and activation energy calculations

Reaction energies and activation barriers for reactions (S1) through (S11) were calculated as described in the main text using equations 11 and 14. The calculated values of $\Delta E_{\mathrm{rxn}}^{\mathrm{liq}}$ for reaction (S1) depend significantly on if and even how H_2O is included. We calculate $\Delta E_{\mathrm{rxn}}^{\mathrm{liq}}$ to be exothermic (0.10 ± 0.08 eV) in the presence of explicit H_2O molecules, exothermic in implicit solvation (-0.29 eV), and more exothermic in the gas phase (-0.56 eV). In contrast, for direct methanol dehydrogenation (reaction (S6)) is for the most part similar, regardless of how H_2O is included in the calculation (using configurations of H_2O molecules or using implicit solvation), or even whether it is included at all. This is because the reaction energy for reaction (S1) is dependent on the change in the interaction energy from the reactant to the product state, which is captured with explicit solvation, while the reaction energy for reaction (S6) is not dependent on the change in interaction energy since the reactant and product states have similar interaction energies.

The ΔE_{act} for reaction (S1) increases substantially from 0.99 eV in the gas phase, to 1.26 eV in the implicit solvent phase, to 1.68 ± 0.18 eV in the explicit solvation phase. A suggestion for this is that there is an added difficulty, and therefore a higher activation barrier, to break this bond in the presence of a water environment. However, the activation barriers for reaction (S6), where the H to be abstracted does not participate in hydrogen-bonding, are similar amongst the different methods. For instance, reaction (S6) has a $\Delta E_{\mathrm{act}} \approx 0.5$ eV regardless of whether it is calculated using explicit solvation, implicit solvation, or in the gas phase. These results are summarized in Table S5.

Table S5: Reaction energies and activation energy barriers for reactions (S1)-(S11). The reported uncertainties are the 95% confidence intervals propagated from the error in the ΔE_{int} over the 10 cMD configurations sampled. Reaction (S8) was neglected from the main text due to a low calculated pre-exponential factor and because all TS searches converged to the TS for reaction (S6).

Reaction	Solvation Model	ΔE_{rxn} [eV]	ΔE_{act} [eV]
(S1): $COH^* + * \longrightarrow CO^* + H^*$	Gas Phase	-0.56	0.99
	Implicit	-0.29	1.26
	Explicit	0.10 ± 0.08	1.68 ± 0.18
(S2): $COH^* + H_2O \longrightarrow COH{-}H_2O^*$	Gas Phase	-0.50	[a]
	Implicit	-0.21	[a]
	Explicit	-0.02 ± 0.15	[a]
(S3): $COH{-}H_2O^* + * \longrightarrow CO^* + H^* + H_2O$	Gas Phase	-0.06	0.00
	Implicit	-0.08	-0.07
	Explicit	0.12 ± 0.13	-0.09 ± 0.13
(S4): $COH{-}H_2O^* + H_2O \longrightarrow COH{-}H_2O{-}H_2O^*$	Gas Phase	-0.01	[a]
	Implicit	0.15	[a]
	Explicit	-0.19 ± 0.22	[a]
(S5): $COH{-}H_2O{-}H_2O^* \longrightarrow CO^* + H_5O_2$	Gas Phase	0.94	0.13
	Implicit	-0.01	0.00
	Explicit	0.22 ± 0.47	0.07 ± 19
(S6): $CH_3OH^* + * \longrightarrow CH_2OH^* + H^*$	Gas Phase	-0.50	0.44
	Implicit	-0.41	0.52
	Explicit	-0.67 ± 0.21	0.34 ± 0.23
(S7): $CH_3OH^* + H_2O \longrightarrow CH_3OH{-}H_2O^*$	Gas Phase	0.37	[a]
	Implicit	0.34	[a]
	Explicit	-0.11 ± 0.28	[a]
(S8): $CH_3OH{-}H_2O^* + * \longrightarrow CH_2OH^* + H^* + H_2O$	Gas Phase	-0.87	[a]
	Implicit	-0.75	[a]
	Explicit	-0.55 ± 0.25	[a]
(S9): $CH_3OH{-}H_2O^* + H_2O \longrightarrow CH_3OH{-}H_2O{-}H_2O^*$	Gas Phase	-0.03	[a]
	Implicit	0.16	[a]
	Explicit	0.33 ± 0.36	[a]
(S10): $CH_3OH{-}H_2O{-}H_2O^* \longrightarrow CH_2OH^* + H_5O_2$	Gas Phase	0.15	0.86
	Implicit	-0.70	[a]
	Explicit	-0.97 ± 0.52	1.23 ± 0.34
(S11): $H_5O_2 + * \longrightarrow 2H_2O + H^*$	Gas Phase	-0.00	-0.94
	Implicit	-0.21	-0.17
	Explicit	0.09 ± 0.46	0.07 ± 0.49

[a] This value was not calculated.

S10.1 All calculated activation barriers

Table S6: Activation energy barriers for dehydrogenation reactions via the direct, H_2O-co-catalyzed, and H_2O-assisted mechanisms. All barriers are calculated in liquid water using explicit solvation. The temperature of the MD simulations used to generate the liquid water configurations was 300 K.

No.	Reaction	ΔE_{act} [eV]	A_{for} [s^{-1}]	K_{eq}
(S1)	$COH^* + * \rightarrow CO^* + H^*$	1.68 ± 0.18	6.25×10^{12}	$(2.48 \pm 7.61) \times 10^{-2}$
(S2)	$COH^* + H_2O \rightarrow COH–H_2O$	~ 0	$(1.43 \pm 0.21) \times 10^{10}$	$(0.26 \pm 1.48) \times 10^{1}$
(S3)	$COH–H_2O + * \rightarrow CO^* + H^* + H_2O$	-0.09 ± 0.13	6.25×10^{12}	$(0.95 \pm 4.82) \times 10^{-2}$
(S2a+S3)	$COH^* + * \overset{H_2O}{\rightarrow} CO^* + H^*$	N/A	$(1.43 \pm 0.21) \times 10^{10}$	$(2.48 \pm 7.61) \times 10^{-2}$
(S4)	$COH^* + 2\ H_2O \rightarrow COH–H_2O–H_2O$	~ 0	$(4.02 \pm 0.03) \times 10^{12}$	$(0.67 \pm 4.17) \times 10^{4}$
(S5)	$COH–H_2O–H_2O \rightarrow CO^* + H_5O_2$	0.11 ± 0.13	6.25×10^{12}	$(0.48 \pm 8.44) \times 10^{-4}$
(S2+S4+S5)	$COH^* + 2\ H_2O \rightarrow CO^* + H_5O_2$	-0.14 ± 0.17	$(4.02 \pm 0.03) \times 10^{12}$	$(0.08 \pm 1.50) \times 10^{1}$
(S6)	$CH_3OH^* + * \rightarrow CH_2OH^* + H^*$	0.34 ± 0.23	6.25×10^{12}	$(0.15 \pm 1.24) \times 10^{12}$
(S7)	$CH_3OH^* + H_2O \rightarrow CH_3OH–H_2O$	~ 0	$(3.00 \pm 1.24) \times 10^{8}$	N/A
(S8)	$CH_3OH–H_2O + * \rightarrow CH_2OH^* + H^* + H_2O$	N/A	6.25×10^{12}	N/A
(S7a+S8)	$CH_3OH^* + * \overset{H_2O}{\rightarrow} CH_2OH^* + H^*$	N/A	$(3.00 \pm 1.24) \times 10^{8}$	$(0.15 \pm 1.24) \times 10^{12}$
(S9)	$CH_3OH^* + 2\ H_2O \rightarrow CH_3OH–H_2O–H_2O$	~ 0	$(6.57 \pm 0.71) \times 10^{9}$	$(0.29 \pm 3.30) \times 10^{2}$
(S10)	$CH_3OH–H_2O–H_2O \rightarrow CH_2OH^* + H_5O_2$	1.53 ± 0.27	6.25×10^{12}	$(0.18 \pm 3.43) \times 10^{12}$
(S7+S9+S10)	$CH_3OH^* + 2\ H_2O \rightarrow CH_2OH^* + H_5O_2$	1.44 ± 0.28	$(6.57 \pm 0.71) \times 10^{9}$	$(0.05 \pm 1.00) \times 10^{14}$
(S11)	$H_5O_2 + * \rightarrow 2\ H_2O + H^*$	0.07 ± 0.49	6.25×10^{12}	$(0.30 \pm 5.26) \times 10^{-1}$

S11 Calculated reaction energies as a function of the number of waters allowed to relax

We performed test calculations where we allowed various numbers of water molecules to relax in the reactant and product configurations for reaction (S1) and report the calculated reaction energies as a function of the number of relaxed water molecules. In these calculations, additional water molecules were included in the relaxation based on their O_{H_2O}—O_{COH*} distance. I.e., for the case where 1 H_2O molecule was relaxed, the H_2O with the shortest O_{H_2O}—O_{COH*} distance was relaxed along with COH*; for the case where 2 H_2O molecules were relaxed, the 2 H_2Os with the shortest O_{H_2O}—O_{COH*} distances were relaxed with COH*; etc.

These calculations were done with two unique water configurations, so the values reported in Figure S28 are the averages of these two sets of calculations. These results indicate that there is only a small change in the reaction energy as long as at least one water molecule is allowed to relax along with the reaction intermediate.

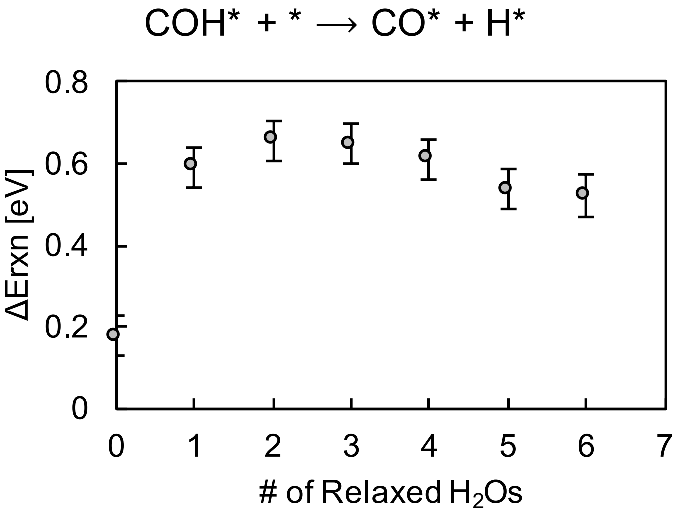

Figure S28: Reaction energy for reaction (S1) as it varies with the number of H_2O molecules that are allowed to relax in the reactant and product geometry optimizations.

S12 Effect of increasing the number of water configurations on calculated TS structures and TS interaction energies

S12.1 TS complex geometries

In this work, we calculated the interaction energy for between 1 and 5 initial geometries of TS complexes for reactions (S1)-(S11). The utility of calculating multiple the interaction energies for multiple geometries appears to be roughly dependent on the relative hydrophilicity or hydrophobicity of the TS complex. For instance, for the reactions following the direct dehydrogenation mechanism (i.e., reactions (S1) and (S6)), we calculated 5 initial geometries of the TS complex under different water configurations. We find that there is smaller variation in the TS complex geometry for reaction (S1) as the average root of sum of squares (RSS) residual in the atomic coordinates is less than 0.1 Å, while the RSS residuals for the TS complex for reaction (S6) is $\sim$ 1.5 Å. This is likely due to the fact that the TS complex for reaction (S1) loses the H from its hydroxyl group, causing it to become more hydrophobic and interact with the surrounding water molecules less strongly, while the TS complex for reaction (S6) contains a hydroxyl group which can hydrogen-bond with liquid water molecules and affect it's binding with the Pt surface. Therefore, it is likely important to consider more initial geometries of TS complexes similar to that for reaction (S6), which has a hydroxyl group that can be involved in hydrogen-bonding if it is pointed up toward to the liquid water, as in the middle panel of Figure S19, or not if it is pointed down towards the Pt surface, as in the middle panel of Figure S22.

The RSS residual for the TS complex geometry for reaction (S1) is smaller than that for reaction (S6). This correlates with an increase in the error of the interaction energy calculation for these two TS complexes. I.e., $\Delta\Delta E_{\mathrm{int}}$ (reaction (S1)) has a 95% confidence interval of 0.06 eV, while $\Delta\Delta E_{\mathrm{int}}$ (reaction (S6)) has a 95% confidence interval of 0.41 eV. For reaction (S1) the average error in the E_{int} for the 5 initial TS complex geometries is 0.16 eV, while for reaction (S6) this error is larger than the average error in the E_{int} for the 5 initial TS complex geometries of 0.15 eV. Therefore, it is necessary to include multiple initial TS complex geometries, especially for reaction (S6), since the error in the interaction energy is not entirely captured unless multiple initial TS complex geometries are considered.

References

[1] D. Cao, G.-Q. Lu, A. Wieckowski, S. A. Wasileski and M. Neurock, *J. Phys. Chem. B*, 2005, **109**, 11622–11633.

[2] X. Nie, W. Luo, M. Janik and A. Asthagiri, *J. Catal.*, 2014, **312**, 108–122.

[3] M. Neurock, S. A. Wasileski and D. Mei, *Chem. Eng. Sci.*, 2004, **59**, 4703–4714.

[4] M. P. Hyman and J. W. Medlin, *J. Phys. Chem. B*, 2006, **110**, 15338–15344.

[5] J. A. Santana, J. J. Mateo and Y. Ishikawa, *J. Phys. Chem. C*, 2010, **114**, 4995–5002.

[6] J. A. Santana, C. R. Cabrera and Y. Ishikawa, *Phys. Chem. Chem. Phys.*, 2010, **12**, 9526–9534.

[7] J. A. Santana, J. J. Saavedra-Arias and Y. Ishikawa, *Electrocatalysis*, 2015, **6**, 534–543.

[8] D. D. Hibbitts, B. T. Loveless, M. Neurock and E. Iglesia, *Angew. Chem., Int. Ed.*, 2013, **52**, 12273–12278.

[9] X. Zhang, T. E. Sewell, B. Glatz, S. Sarupria and R. B. Getman, *Catal. Today*, 2017, **285**, 57–64.

[10] S. K. Desai, V. Pallassana and M. Neurock, *J. Phys. Chem. B*, 2001, **105**, 9171–9182.

[11] T. Xie, C. J. Bodenschatz and R. B. Getman, *React. Chem. Eng.*, 2019, **4**, 383–392.

[12] C. Hartnig and E. Spohr, *Chem. Phys.*, 2005, **319**, 185–191.

[13] S. Desai and M. Neurock, *Electrochim. Acta*, 2003, **48**, 3759 – 3773.

[14] C. Hartnig, J. Grimminger and E. Spohr, *J. Electroanal. Chem.*, 2007, **607**, 133–139.

[15] C. Hartnig, J. Grimminger and E. Spohr, *Electrochim. Acta*, 2007, **52**, 2236–2243.

[16] T. Xie, S. Sarupria and R. B. Getman, *Mol. Sim.*, 2017, **43**, 370–378.

[17] X. Zhang, R. S. DeFever, S. Sarupria and R. B. Getman, *J. Chem. Inf. Model.*, 2019, **In Press**.

[18] G. Kresse and J. Hafner, *Phys. Rev. B*, 1993, **47**, 558.

[19] G. Kresse and J. Hafner, *Phys. Rev. B*, 1994, **49**, 14251.

[20] G. Kresse and J. Furthmüller, *Comput. Mater. Sci.*, 1996, **6**, 15–50.

[21] G. Kresse and J. Furthmüller, *Phys. Rev. B*, 1996, **54**, 11169.

[22] J. P. Perdew, K. Burke and M. Ernzerhof, *Phys. Rev. Lett.*, 1996, **77**, 3865.

[23] J. P. Perdew, K. Burke and M. Ernzerhof, *Phys. Rev. Lett.*, 1997, **78**, 1396.

[24] P. E. Blöchl, *Phys. Rev. B*, 1994, **50**, 17953.

[25] G. Kresse and D. Joubert, *Phys. Rev. B*, 1999, **59**, 1758.

[26] S. Grimme, *J. Comput. Chem.*, 2006, **27**, 1787–1799.

[27] H. J. Monkhorst and J. D. Pack, *Phys. Rev. B*, 1976, **13**, 5188.

[28] S. Nosé, *Mol. Phys.*, 1984, **52**, 255–268.

[29] W. G. Hoover, *Phys. Rev. A*, 1985, **31**, 1695–1697.

[30] A. D. MacKerell, D. Bashford, M. Bellott, R. Dunbrack, J. D. Evanseck, M. J. Field, S. Fischer, J. Gao, H. Guo, S. Ha *et al.*, *J. Phys. Chem. B*, 1998, **102**, 3586–3616.

[31] A. K. Rappé, C. J. Casewit, K. Colwell, W. Goddard Iii and W. Skiff, *J. Am. Chem. Soc.*, 1992, **114**, 10024–10035.

[32] L. X. Dang and B. M. Pettitt, *J. Phys. Chem.*, 1987, **91**, 3349–3354.

[33] S. N. Steinmann, R. Ferreira De Morais, A. W. GÃűtz, P. Fleurat-Lessard, M. Iannuzzi, P. Sautet and C. Michel, *J. Chem. Theory Comput.*, 2018, **14**, 3238–3251.

[34] S. Cui, J. Liu, M. E. Selvan, D. J. Keffer, B. J. Edwards and W. V. Steele, *J. Phys. Chem. B*, 2007, **111**, 2208–2218.

[35] T. A. Manz and D. S. Sholl, *J. Chem. Theory Comput.*, 2010, **6**, 2455–2468.

[36] K. Kahn and T. C. Bruice, *J. Comput. Chem.*, 2002, **23**, 977–996.

[37] W. L. Jorgensen, D. S. Maxwell and J. Tirado-Rives, *J. Am. Chem. Soc.*, 1996, **118**, 11225–11236.

[38] W. L. Jorgensen and J. Tirado-Rives, *PNAS*, 2005, **102**, 6665–6670.

[39] C. J. Bodenschatz, X. Zhang, T. Xie, J. Arvay, S. Sarupria and R. B. Getman, *J. Visualized Exp.*, 2019, **In Press**.

[40] W. L. Jorgensen and C. Jenson, *J. Comput. Chem.*, 1998, **19**, 1179–1186.

[41] G. Henkelman and H. Jonsson, *J. Chem. Phys.*, 2000, **113**, 9901–9904.

[42] G. Henkelman and H. Jonsson, *J. Chem. Phys.*, 2000, **113**, 9978–9985.